Title

High-Plex Spatial RNA Profiling Reveals Cell Type–Specific Biomarker Expression during Melanoma Development

Journal

Journal of Investigative Dermatology, 142(5)

ISSN

0022-202X

Authors

Kiuru, Maija

Kriner, Michelle A

Wong, Samantha

et al.

Publication Date

2022-05-01

DOI

10.1016/j.jid.2021.06.041

Peer reviewed

HHS Public Access

Author manuscript

J Invest Dermatol. Author manuscript; available in PMC 2023 May 01.

Published in final edited form as:

J Invest Dermatol. 2022 May ; 142(5): 1401–1412.e20. doi:10.1016/j.jid.2021.06.041.

High-plex spatial RNA profiling reveals cell type-specific biomarker expression during melanoma development

Maija Kiuru[1,2,*], **Michelle A. Kriner**[3,*], **Samantha Wong**[1], **Guannan Zhu**[1,4], **Jessica R. Terrell**[1], **Qian Li**[5], **Margaret Hoang**[3], **Joseph Beechem**[3], **John D. McPherson**[6]

[1]Department of Dermatology, University of California Davis, Sacramento, California, USA

[2]Department of Pathology & Laboratory Medicine, University of California Davis, Sacramento, California, USA

[3]NanoString Technologies, Inc., Seattle, Washington, USA

[4]Department of Dermatology, Xijing Hospital, Fourth Military Medical University, Xi'an, Shaanxi, China

[5]Center for Oncology Hematology Outcomes Research and Training (COHORT) and Division of Hematology and Oncology, University of California, Davis, Sacramento, CA

[6]Department of Biochemistry & Molecular Medicine, University of California Davis, Sacramento, California, USA

Abstract

Early diagnosis of melanoma is critical for improved survival. However, biomarkers of early melanoma evolution and their origin within the tumor and its microenvironment, including the keratinocytes, are poorly defined. To address this, we used spatial transcript profiling that maintains the morphological tumor context to measure expression of >1,000 RNAs *in situ* in patient-derived formalin-fixed, paraffin-embedded tissue sections in primary melanoma and melanocytic nevi. We profiled 134 200μm-diameter regions of interest enriched in melanocytes, neighboring keratinocytes or immune cells. This approach captured distinct expression patterns across cell types and tumor types during melanoma development. Unexpectedly, we discovered that *S100A8* is expressed by keratinocytes within the tumor microenvironment during melanoma growth. Immunohistochemistry of 252 tumors showed prominent keratinocyte-derived S100A8 expression in melanoma but not in benign tumors and confirmed the same pattern for S100A8's binding partner S100A9, suggesting that injury to the epidermis may be an early and readily

Corresponding author: Maija Kiuru, Department of Dermatology, University of California, Davis, 3301 C Street, Suite 1400, Sacramento, CA 95816, tel: +1-916-551-2686, mkiuru@ucdavis.edu, Twitter handle: @maijakiuru, Instagram handle: @dr.maija.

*These authors contributed equally

AUTHOR CONTRIBUTIONS

Conceptualization: M.K., J.D.M., M.H. and M.A.K.; Analysis: M.K., M.A.K., Q.L.; Investigation: M.K., M.A.K., J.D.M., M.H., G.Z., J.R.T., S.W.; Methodology: J.B.; Resources: J.B.; Writing - Original Draft Preparation: M.K. and M.A.K.; Writing - Review and Editing: M.K., M.A.K., S.W., G.Z., J.R.T., Q.L., M.H., J.B., J.D.M.

Conflict of interest: M.A.K., M.H. and J.B. are employees and stockholders of NanoString Technologies.

detectable indicator of melanoma development. Together, our results establish a framework for high-plex, spatial and cell type-specific resolution of gene expression in archival tissue applicable to the development of biomarkers and characterization of tumor-microenvironment interactions in tumor evolution.

INTRODUCTION

Melanoma, the deadliest of the common skin cancers, is curable with early diagnosis and treatment (Gershenwald et al., 2017). However, histopathologic diagnosis of melanoma can be complicated by morphological mimicry, especially its early forms, by a subset of melanocytic nevi. Because development of melanoma is a stepwise process in which melanocytes accrue mutations and escape environmental controls on proliferation (Villanueva and Herlyn, 2008), understanding the interaction of melanocytes with neighboring cell types is crucial to development of diagnostic tools and effective treatments.

Many melanoma-associated genes have been identified (Bastian, 2014, Charbel et al., 2014, Roh et al., 2015, Shain and Bastian, 2016, Shain et al., 2015) and molecular tests for diagnosis and prognosis melanoma are gradually being introduced (Clarke et al., 2015, Gerami et al., 2015a, Gerami et al., 2015b), but markers of early melanoma development, including within the tumor microenvironment, remain lacking. In addition, although the treatment of metastatic melanoma has changed drastically since the development of immune checkpoint inhibitor therapies (Khair et al., 2019), biomarkers predicting durable treatment response are largely unknown. Given the heterogeneity, low cellularity and spatial context of immune and microenvironment responses (Finotello and Eduati, 2018), spatially resolved techniques are likely to outperform bulk molecular profiling for discovery of early stage and predictive biomarkers.

Previous studies have revealed the importance of keratinocyte-derived growth factors and cell adhesion molecules in limiting melanocyte proliferation in normal skin and elucidated mechanisms by which malignant melanocytes escape this regulation (Haass et al., 2005, Villanueva and Herlyn, 2008). However, these experiments relied on the use of co-culture systems or heterologous expression of keratinocyte-derived genes in melanocytes, neither of which capture the spatial element of melanocyte-keratinocyte interactions *in situ*. Furthermore, single-cell RNA sequencing (scRNAseq) studies on melanoma have largely focused on melanoma metastases, overlooking the keratinocyte microenvironment of primary melanomas (Jerby-Arnon et al., 2018, Tirosh et al., 2016). Since scRNAseq rely on fresh tissue, studies on benign melanocytic tumors in humans are also lacking.

To address the challenges outlined above, we took a discovery-based approach for studying tumor-microenvironment interactions during melanoma evolution within the native morphological context of the tumor, including within the keratinocyte microenvironment. Specifically, we examined expression of over 1,000 genes (Supplementary Table S1) in 134 regions of interest (ROIs) enriched for melanocytes, neighboring keratinocytes or immune cells in patient-derived formalin-fixed, paraffin-embedded (FFPE) tissue sections from 12 melanocytic tumors, ranging from benign to malignant, using the NanoString GeoMx® Digital Spatial Profiler (DSP) (Beechem, 2020) (Figure 1). We discovered that the damage-

associated molecular pattern (DAMP) *S100A8*, which is a known melanoma marker (10) thought to be expressed by immune cells (18), is keratinocyte-derived in melanoma and confirmed this finding by immunohistochemistry (IHC) in a cohort of 252 melanomas.

RESULTS

Cell type & case type both influence the expression profile of each ROI

We validated the technical performance of DSP on one FFPE tissue from each of four case types (common nevi, CN; dysplastic nevi, DN; melanoma *in situ*, MIS; invasive melanoma, MM), observing high reproducibility across replicate experiments and expected gene expression patterns across ROI types using a 108-gene test panel (1,048 probes; 10 probes per gene for most genes; Supplementary Figure 1). Next, we used a 1,412-gene panel (4,998 probes; 3 probes per gene for most genes) to profile three tumors per case type. Two of the three melanoma cases were Stage pT1a and the third was Stage pT2b. We selected 6–16 200μm diameter circular ROIs in each tissue, with 134 ROIs in total (Supplementary Figure 2). One keratinocyte-rich ROI on the periphery of each tissue was chosen to serve as a “normal” control (Figure 2A). To facilitate comparison across tissues, we assigned all other ROIs to one of five categories (immune-rich, melanocyte-rich, immune/melanocyte-rich, keratinocyte/melanocyte-rich or mixed) (Figure 2A) and evaluated the cell type composition of each ROI (Figure 2B). Raw counts were normalized to the upper quartile (Bullard et al., 2010) for each ROI to enable comparison across ROIs.

To further validate the performance of DSP, we examined expression of known melanomagenesis-associated genes across the cohort. We observed that the melanoma biomarker *PRAME* (preferentially expressed antigen in melanoma) (Clarke et al., 2015, Gerami et al., 2017) and the melanoma-associated developmental marker *PMEL* (Sarantou et al., 1997) were significantly and specifically elevated in melanocyte-containing ROIs in the three invasive melanoma cases (Figure 2C). *KRT14* and *CXCL14* (Riker et al., 2008) were elevated in keratinocyte-containing ROIs relative to melanocyte-rich or immune-rich ROIs in all four tumor types and were further upregulated in the melanomas (Figure 2C). Finally, the pan-leukocyte marker *PTPRC* (CD45) and the T cell chemoattractant gene *CXCL9*, which are included in a gene expression-based diagnostic test for melanoma (Clarke et al., 2015), were detected specifically in immune-rich ROIs, particularly in melanomas (Figure 2C). Together, these results validated prior data and also revealed cell-type specific expression of known melanoma biomarkers.

Unbiased clustering of ROIs based on pairwise correlation coefficients revealed that cell type and tumor type both affect the similarity between ROIs (Figure 2D). The ROIs clustered into five groups, two of which consisted of melanocyte-rich ROIs (Figure 2D; M1, M2), two of which consisted immune-rich ROIs (Figure 2D; I1, I2) and one of which consisted of keratinocyte-rich ROIs (Figure 2D; K). For the M and I clusters, the differences between groups 1&2 were based on case type: M1 and I1 contained only melanoma or melanoma *in situ* ROIs, while M2 and I2 had no melanoma ROIs (Figure 2D). The K cluster contained all 12 control keratinocyte ROIs and most of the mixed keratinocyte/melanocyte ROIs, suggesting that keratinocyte-specific genes drive clustering of these ROIs.

A framework for identification of cell type-specific gene expression

Because the I1 and M1 clusters were composed entirely of ROIs from the melanoma or melanoma in situ cases, genes expressed only in these clusters have biomarker potential. Importantly, since ROIs were selected based on enrichment of certain cell populations, we were able to perform a cell type-specific analysis. We performed linear regression to identify genes that were 1) significantly enriched in M1 or I1 ROIs compared to other ROIs containing the same cell type(s) and 2) not detected in any ROIs from common nevi. For M1, the known biomarker *PRAME* was by far the most significantly enriched gene (Figure 3A). The other top hits *LEF1*, *CD276*, *BCL2A1* and *SLC7A5* have been shown to be up-regulated or amplified in melanoma but are also detectable in benign nevi or normal melanocytes (Haq et al., 2013, Tekle et al., 2012, Wang et al., 2014, Xu et al., 2015). For the immune ROIs in I1, the two most highly enriched genes in melanoma that were also not detected in nevi were *PTPRC* and *CXCL9* (Figure 3B), followed by genes broadly related to leukocyte biology (Figure 3B), including MHC II antigen presentation (*HLA-Dxx*, *CTSS*).

Enrichment analysis does not provide information on the relationship of genes to each other, so to further leverage the spatial resolution of DSP data we used the dimensionality reduction technique UMAP to visualize the relative spatial expression profiles of all genes (Figure 3C–D). This approach can be used to determine which genes tend to be expressed in the same location (or not), a property that is lost in bulk measurements such as RNA-seq. Importantly, marker genes with different spatial expression profiles can provide orthogonal information, whereas genes with the same expression profile are more likely to be reporting on similar biology. We chose UMAP over other methods such as t-SNE because it preserves both local and global data structure and captures meaningful biological relationships (Becht et al., 2018). At the global level, UMAP analysis produced three gene clusters on the left side of the plot space and we validated the UMAP output by confirming that gene clustering correlated with cell type (Figure 3C, colored dots) and tumor type (Figure 3D, colored dots).

Notably, the expression profiles of *PMEL*, *CTNNB1*, *LDHB* and *CDK2* were more similar to *PRAME* than the genes enriched in melanoma melanocytes (Figure 3C vs. D), but of these genes only *CDK2* was not detected in nevi (Figure 3E). Genes enriched in melanoma immune ROIs were not tightly UMAP-adjacent (Figure 3C); instead they clustered next to genes expressed by the same cell type or within same pathway (Figure 3D; for example, *PTPRC* and *LCP1* are expressed by lymphocytes, *HLA-DMA* and *HLA-DQA1/2* by antigen-presenting cells, *CXCL9* with other interferon gamma-stimulated genes such as *GBP1*). All of these genes were primarily detected in MIS or MM (Figure 3F). The gene signatures shown in Figure 3E/F were both predictive of cell type and case type (Supplementary Figure 3).

Together, these results established a framework for identification of cell type-specific gene expression during melanoma evolution.

Analysis of intermediate ROI clusters reveals components of the keratinocyte microenvironment in melanoma

Since the K1/M2 clusters encompass most epidermal keratinocyte-containing ROIs (Figure 2D), we reasoned that K1/M2 might reveal markers of melanoma *in situ*, which grows within the epidermis. We performed linear regression comparing the seven malignant ROIs in vs. all other ROIs in K1 and M2. The most highly enriched gene in this analysis that was also not detected in common nevi was the S100 calcium binding protein family member and DAMP *S100A8* (Figure 4A).

We determined by IHC that S100A8 is expressed by keratinocytes rather than melanocytes (Figure 4B), yet *S100A8* was most strongly expressed in ROIs containing >50% melanocytes rather than >50% keratinocytes (Figure 4C), suggesting that keratinocytes may express *S100A8* in response to consumption of the epidermis by malignant melanocytes. Indeed, we observed that the ROIs with the highest *S100A8* expression had melanocytes scattered throughout the epidermis, a histopathologic feature of melanoma *in situ* (Figure 4D). Expression of *S100A8* was not strongly correlated with keratinocyte content (Figure 4D), further indicating that high S100A8 expression is not merely a function of keratinocyte abundance. *KRT17* and *KRT6A-B-C* were the closest points to *S100A8* in UMAP space, and indeed these genes were enriched in the same ROIs (Figure 4F). This profile was not seen for other keratins such as *KRT14* (Figure 4F). *KRT17* and *KRT6* are known to be upregulated in wounded skin (Zhang et al., 2019); thus enrichment of these genes in the same ROIs as *S100A8* supports the notion that the growth of melanoma *in situ* within the epidermis elicits an injury response within the keratinocytes.

S100A8/A9 are detected in the keratinocyte microenvironment of melanoma

To further validate the data from spatial transcript profiling, we performed S100A8 IHC on an independent cohort of 252 melanocytic tumors (68 CN, 66 DN, 69 MIS, 49 MM; Table 1). S100A8 expression was scored based on the percentage of epidermis expressing S100A8 that was directly associated with the tumor (epidermis containing tumor and/or epidermis overlying intradermal tumor; a schematic of the scoring in Supplementary Figure 4). Notably, the keratinocyte microenvironment of melanoma (Figure 5A–B, Supplementary Figure 5) and many cases of melanoma *in situ* (Figure 5C–D) showed prominent expression of S100A8, while the keratinocyte microenvironment of most dysplastic nevi (Figure 5E–F) and common nevi (Figure 5G–H, Supplementary Figure 5) lacked or had only limited staining (Table 2, $p<0.001$; Figure 5I, AUC 0.83; representative images of scores 1–5 in Supplementary Figure 6). A binary logistic regression model showed that increased S100A8 IHC score was significantly associated with invasive melanoma tumor type (OR=2.49, 95%CI 1.93–3.21) and remained significant after adjusting for sex, anatomic site and age (OR=2.54, 95%CI 1.92–3.36). S100A8 expression was also apparent in scattered immune cells within the dermis of both nevi and melanoma as well as within the normal hair follicle epithelium (Figure 5, Supplementary Figure 5), but this expression was not taken into account when scoring S100A8 staining. Remarkably, if the tumor showed “skip areas,” i.e., areas of uninvolved skin, the epidermis lacked S100A8 expression in these foci (Figure 5J).

S100A8 is generally co-expressed with S100A9, forming a complex known as calprotectin (Gebhardt et al., 2006). Because the DSP probe pool used in our experiments did not target *S100A9* and our S100A8 antibody (CF-145) is not cross-reactive, we analyzed the expression of S100A9 in a subset of tumors by immunohistochemistry. Similar to S100A8, S100A9 was expressed by the keratinocytes associated with melanoma but not nevi (Supplementary Figure 7, Supplementary Table 2). Together, these data demonstrate that epidermal keratinocytes express S100A8/A9 in response to melanoma growth, revealing the cellular origin of a melanoma biomarker within the tumor microenvironment and emphasizing the interaction between melanoma and the keratinocyte microenvironment.

DISCUSSION

Melanoma is the fifth most common cancer type in the United States and causes the vast majority of skin cancer deaths (Surveillance, 2019). Despite advances in immunotherapy, markers predicting sustained treatment response are inadequate. Understanding the interplay between melanocytes and neighboring keratinocytes and immune cells will be crucial to the development of improved diagnostic and prognostic tools and therapeutic targets. We aimed to study tumor-microenvironment interactions in melanoma within their native morphological context using GeoMx DSP.

After validating the performance and reproducibility of the DSP assay on our FFPE tissue sections, we profiled 134 ROIs in a cohort of 12 common benign and malignant melanocytic tumors with a panel that targets 1,400+ immune-oncology-related genes. We detected over 900 targets with high confidence in a single experiment, which would traditionally require tedious microdissection or be limited to a few genes (Wang et al., 2012). Other technologies for transcriptome-scale spatial profiling have recently been applied to melanoma, but our experiment detected approximately ten times more transcripts per square micron than a recent study (Thrane et al., 2018). Importantly, the compatibility of GeoMx DSP with FFPE enables profiling of archival tissues (all specimens in our study were at least two years old), which has been especially difficult for skin samples (Kwong et al., 2018). This is particularly important for the study of melanoma evolution in patient-derived benign and malignant primary tumors and the keratinocyte microenvironment, which have been mainly overlooked in scRNAseq studies of melanoma.(Jerby-Arnon et al., 2018, Tirosh et al., 2016)

A cell type-enriched ROI selection strategy enabled us to directly compare similar cell populations across tumors when looking for gene enrichment in melanomas (Figure 2–3). This approach, coupled with a dimensionality reduction-based approach to identify co-expressed genes, successfully identified known melanoma-associated markers and demonstrated their specificity to melanocytes, immune infiltrates or the epidermal (keratinocyte) microenvironment (Figure 3–4). Interestingly, genes enriched in melanocytes (*PRAME*), keratinocytes (*S100A8*) or immune cells (*PTPRC, CXCL9*) in our study correspond with the three components of a commercially available diagnostic test; our results may explain why the three components do not correlate well with each other and are all required to generate the most predictive score (Clarke et al., 2015).

Importantly, a published bulk RNA-seq dataset comparing 57 melanomas and 23 nevi (Kunz et al., 2018) both validates our data and highlights the advantages of a spatially resolved, cell type-specific analysis, especially regarding the tumor microenvironment. While the melanoma markers specific to melanocyte ROIs were also melanoma-enriched in the bulk RNA-seq data, markers of the immune and keratinocyte microenvironment were not as strongly melanoma-associated (Supplementary Figure 8), likely reflecting masking of less abundant cell types in bulk measurements. By contrast, enrichment of these gene sets in melanoma was of similar magnitude for melanocyte- vs. immune-associated genes in the DSP data (Figure 3A–B), suggesting that this technology may be more sensitive for identifying gene products that originate from non-tumor cells in the tumor microenvironment. In fact, a recent study using GeoMx DSP to study protein expression in melanoma found that expression of PD-L1 in macrophages, rather than tumor cells, was predictive of response to immunotherapy (Toki et al., 2019). Because understanding of tumor-microenvironment interactions in melanoma is much needed in the era of melanoma immunotherapy, additional studies are warranted to validate the genes enriched in melanoma immune infiltrates in our DSP cohort.

S100A8 is a DAMP that has multiple roles in promoting immune responses and inflammation (Nukui et al., 2008, Srikrishna, 2012). It is most well-known as part of the S100A8/A9 complex (calprotectin), which is canonically expressed and secreted by neutrophils, monocytes and macrophages (Gebhardt et al., 2006). *S100A8/A9* is also upregulated in a number of inflammatory disorders such as psoriasis and cystic fibrosis (Gebhardt et al., 2006, Nukui et al., 2008) and expressed in a variety of epithelial tumor types (Gebhardt et al., 2006), where it is associated with invasiveness and poor prognosis (Arai et al., 2008). While upregulation of *S100A8/A9* in melanoma has been established using bulk methods (Clarke et al., 2015, Kunz et al., 2018, Wagner et al., 2019), previous studies have assumed that it is expressed by immune cells (Clarke et al., 2015, Wagner et al., 2019). Our analysis reveals the keratinocyte-derived origin of *S100A8/A9* during melanoma development (Figure 4A–C, Figure 5, Table 2, Supplementary Figures 5–7). This observation may explain why *S100A8/A9* is strongly detected in primary melanomas but not metastases (Xiong et al., 2019). Furthermore, it emphasizes the importance of understanding a biomarker's cellular origin, as non-cutaneous metastasis and micro-dissected tumors may lack keratinocytes and thus produce falsely low expression levels of *S100A8/A9* in current commercially available tests. In addition, expression of *S100A8/A9* specifically at the skin surface in early melanoma could potentially be exploited to increase the sensitivity of an adhesive patch biopsy assay, similar to that which is already available for *PRAME* (Gerami et al., 2017). Lastly, the results suggest a potential role for S100A8 IHC as an ancillary test for the diagnosis of melanoma, especially as IHC-based testing can be readily adopted for use in most pathology laboratories.

Due to the correlation of *S100A8* expression with melanocyte growth within the epidermis (Figure 4B–D) and expression of the wound-associated keratins 6 and 17 (Figure 4E), *S100A8* expression in this context may be a response to inflammation or destruction of the epidermis by the melanocytes. This notion is supported by prior literature on S100A8 being expressed in epithelial cells in response to stress and inflammation (Kerkhoff et al., 2012). Cytokines secreted by nearby tumor cells likely play a role as well, since keratinocytes

overlying melanoma purely within the dermis also strongly expressed S100A8 (Figure 5) and multiple cytokines are known to induce *S100A8* in normal keratinocytes (Nukui et al., 2008). Because S100A8/A9 is a chemoattractant for melanocytes that express certain cell adhesion molecules such as MCAM, ALCAM and RAGE (Ruma et al., 2016), induction of *S100A8* in the epidermis may stimulate melanocyte migration; indeed, S100A8/A9 have been implicated in metastasis of melanoma and other tumor types (Arai et al., 2008, Ruma et al., 2016, Saha et al., 2010). Additional DSP studies profiling a larger number of patients and ROIs are warranted to further resolve the interplay between keratinocytes and melanocytes during melanomagenesis.

MATERIALS AND METHODS

See Supplementary Materials and Methods for more details.

Cases

This study was approved and a waiver of the informed consent requirement was granted by the institutional review board of University of California Davis as specimens were deidentified. Pathology archives were searched for CN, DN, MIS, and MM and archived hematoxylin and eosin (H&E) stained sections were reviewed by a dermatopathologist (M.K.) to confirm diagnoses.

Five μm thick serial sections derived from FFPE tissue blocks were cut. One section was stained with H&E and two unstained sections were mounted on positively charged histology slides for in situ hybridization and DSP. Whole slide imaging of the H&E sections was performed on a Nikon TE2000-E microscope and ROIs representative of the tumor and its microenvironment were selected by the pathologist.

In situ hybridization

See Supplementary Materials and Methods for details.

Digital spatial profiling

Slides were blocked for 30 min as described (Merritt et al., 2019) and then incubated with 300 nM Syto13 and fluorescently conjugated antibodies to CD3, S100B, Pmel and CD45 for 1h and washed in 2X SSC. Slides were loaded onto a DSP instrument and submerged/ washed in PBS with 0.1% Tween 20 as described (Merritt et al., 2019). Following 20x fluorescence scanning to obtain a high-resolution image of the tissue, ROIs were selected by matching to the pathologist- selected regions on the H&E-stained serial section. Between six and 16 ROIs were chosen per tissue (all 200 μm diameter circles). Indexing oligos were released from each ROI by exposure to UV light as described (Merritt et al., 2019) and 10 μl of liquid from above the ROI was collected by a microcapillary tip and deposited in a 96-well plate.

Library preparation & sequencing

Indexing oligos from each ROI were PCR amplified using primers that 1) hybridize to constant regions and 2) contain unique dual-indexed barcoding sequences to preserve ROI

identity. PCR products were pooled and purified twice with Ampure XP beads (Beckman Coulter). Library concentration and purity were measured using a high sensitivity DNA Bioanalyzer chip (Agilent). Paired end (2 × 75 bp reads) sequencing was performed on an Illumina MiSeq instrument (pilot experiment) or Illumina HiSeq 2500 instrument (full panel experiment).

Data processing

See Supplementary Materials and Methods for details.

Data analysis

A high confidence detection threshold was set at the geometric mean plus 2.5 standard deviations of the negative probes. 923 of 1,412 genes (65%) in the full panel were above the detection threshold in at least one ROI. The 489 genes below the detection threshold in all ROIs were excluded from further analysis.

Immunohistochemistry

S100A8 mouse monoclonal antibody [CF-145] (catalog # 14–9745-82, eBioscience) and S100A9 mouse monoclonal antibody [Clone #747315] (catalog # MAB5578-SP, R&D Systems) were used. Staining was scored with 100% consensus agreement by two observers (M.K., S.W.) based on the percentage of epidermis stained that is directly associated with the tumor, using a previously described scoring system with appropriate modifications (42): score 1= 0–5%; score 2= 6% to 25%; score 3= 26% to 50%; score 4= 51% to 75%; score 5=>75% (Supplementary Figure 3).

Supplementary Material

Refer to Web version on PubMed Central for supplementary material.

ACKNOWLEDGMENTS

We thank Lan Yu, Aubrey Gasper, Daniel Gong, and Roberta Tibbett for technical assistance with this study. M.K. acknowledges support from the Dermatology Foundation, through Career Development Award in Dermatopathology and the National Institute of Arthritis and Musculoskeletal and Skin Diseases, National Institutes of Health through grant #K23AR074530.

DATA AVAILABILITY STATEMENT

Datasets related to this article can be found at https://www.ncbi.nlm.nih.gov/geo/ using the accession number GSE168013.

Abbreviations:

ROI	regions of interest
FFPE	formalin-fixed, paraffin-embedded
CN	common nevi
DN	dysplastic nevi

MIS	melanoma *in situ*
MM	invasive melanoma
DSP	digital spatial profiler
IHC	immunohistochemistry

REFERENCES

Arai K, Takano S, Teratani T, Ito Y, Yamada T, Nozawa R. S100A8 and S100A9 overexpression is associated with poor pathological parameters in invasive ductal carcinoma of the breast. Curr Cancer Drug Targets 2008;8(4):243–52. [PubMed: 18537548]

Bastian BC. The molecular pathology of melanoma: an integrated taxonomy of melanocytic neoplasia. Annu Rev Pathol 2014;9:239–71. [PubMed: 24460190]

Becht E, McInnes L, Healy J, Dutertre CA, Kwok IWH, Ng LG, et al. Dimensionality reduction for visualizing single-cell data using UMAP. Nat Biotechnol 2018.

Beechem JM. High-Plex Spatially Resolved RNA and Protein Detection Using Digital Spatial Profiling: A Technology Designed for Immuno-oncology Biomarker Discovery and Translational Research. In: Thurin M, Cesano A, Marincola FM, editors. Biomarkers for Immunotherapy of Cancer: Methods and Protocols New York, NY: Springer New York; 2020. p. 563–83.

Bullard JH, Purdom E, Hansen KD, Dudoit S. Evaluation of statistical methods for normalization and differential expression in mRNA-Seq experiments. BMC Bioinformatics 2010;11:94. [PubMed: 20167110]

Charbel C, Fontaine RH, Malouf GG, Picard A, Kadlub N, El-Murr N, et al. NRAS mutation is the sole recurrent somatic mutation in large congenital melanocytic nevi. J Invest Dermatol 2014;134(4):1067–74. [PubMed: 24129063]

Clarke LE, Warf MB, Flake DD 2nd, Hartman AR, Tahan S, Shea CR, et al. Clinical validation of a gene expression signature that differentiates benign nevi from malignant melanoma. J Cutan Pathol 2015;42(4):244–52. [PubMed: 25727210]

Finotello F, Eduati F. Multi-Omics Profiling of the Tumor Microenvironment: Paving the Way to Precision Immuno-Oncology. Frontiers in Oncology 2018;8(430).

Gebhardt C, Nemeth J, Angel P, Hess J. S100A8 and S100A9 in inflammation and cancer. Biochem Pharmacol 2006;72(11):1622–31. [PubMed: 16846592]

Gerami P, Cook RW, Russell MC, Wilkinson J, Amaria RN, Gonzalez R, et al. Gene expression profiling for molecular staging of cutaneous melanoma in patients undergoing sentinel lymph node biopsy. J Am Acad Dermatol 2015a;72(5):780–5 e3. [PubMed: 25748297]

Gerami P, Cook RW, Wilkinson J, Russell MC, Dhillon N, Amaria RN, et al. Development of a prognostic genetic signature to predict the metastatic risk associated with cutaneous melanoma. Clin Cancer Res 2015b;21(1):175–83. [PubMed: 25564571]

Gerami P, Yao Z, Polsky D, Jansen B, Busam K, Ho J, et al. Development and validation of a noninvasive 2-gene molecular assay for cutaneous melanoma. J Am Acad Dermatol 2017;76(1):114–20 e2. [PubMed: 27707590]

Gershenwald JE, Scolyer RA, Hess KR, Sondak VK, Long GV, Ross MI, et al. Melanoma staging: Evidence-based changes in the American Joint Committee on Cancer eighth edition cancer staging manual. CA Cancer J Clin 2017;67(6):472–92. [PubMed: 29028110]

Haass NK, Smalley KS, Li L, Herlyn M. Adhesion, migration and communication in melanocytes and melanoma. Pigment Cell Res 2005;18(3):150–9. [PubMed: 15892711]

Haq R, Yokoyama S, Hawryluk EB, Jonsson GB, Frederick DT, McHenry K, et al. BCL2A1 is a lineage-specific antiapoptotic melanoma oncogene that confers resistance to BRAF inhibition. Proc Natl Acad Sci U S A 2013;110(11):4321–6. [PubMed: 23447565]

Jerby-Arnon L, Shah P, Cuoco MS, Rodman C, Su MJ, Melms JC, et al. A Cancer Cell Program Promotes T Cell Exclusion and Resistance to Checkpoint Blockade. Cell 2018;175(4):984–97 e24. [PubMed: 30388455]

Kerkhoff C, Voss A, Scholzen TE, Averill MM, Zänker KS, Bornfeldt KE. Novel insights into the role of S100A8/A9 in skin biology. Exp Dermatol 2012;21(11):822–6. [PubMed: 22882537]

Khair DO, Bax HJ, Mele S, Crescioli S, Pellizzari G, Khiabany A, et al. Combining Immune Checkpoint Inhibitors: Established and Emerging Targets and Strategies to Improve Outcomes in Melanoma. Frontiers in Immunology 2019;10(453).

Kunz M, Loffler-Wirth H, Dannemann M, Willscher E, Doose G, Kelso J, et al. RNA-seq analysis identifies different transcriptomic types and developmental trajectories of primary melanomas. Oncogene 2018;37(47):6136–51. [PubMed: 29995873]

Kwong LN, De Macedo MP, Haydu L, Joon AY, Tetzlaff MT, Calderone TL, et al. Biological Validation of RNA Sequencing Data from Formalin-Fixed Paraffin-Embedded Primary Melanomas. JCO Precis Oncol 2018;2018.

Merritt CR, Ong GT, Church SE, Barker K, Danaher P, Geiss G, et al. Multiplex digital spatial profiling of proteins and RNA in fixed tissue. Nat Biotechnol 2020;38(5):586–599. [PubMed: 32393914]

Nukui T, Ehama R, Sakaguchi M, Sonegawa H, Katagiri C, Hibino T, et al. S100A8/A9, a key mediator for positive feedback growth stimulation of normal human keratinocytes. J Cell Biochem 2008;104(2):453–64. [PubMed: 18044712]

Passarelli A, Mannavola F, Stucci LS, Tucci M, Silvestris F. Immune system and melanoma biology: a balance between immunosurveillance and immune escape. Oncotarget 2017;8(62):106132–42. [PubMed: 29285320]

Riker AI, Enkemann SA, Fodstad O, Liu S, Ren S, Morris C, et al. The gene expression profiles of primary and metastatic melanoma yields a transition point of tumor progression and metastasis. BMC Med Genomics 2008;1:13. [PubMed: 18442402]

Roh MR, Eliades P, Gupta S, Tsao H. Genetics of melanocytic nevi. Pigment Cell Melanoma Res 2015;28(6):661–72. [PubMed: 26300491]

Ruma IM, Putranto EW, Kondo E, Murata H, Watanabe M, Huang P, et al. MCAM, as a novel receptor for S100A8/A9, mediates progression of malignant melanoma through prominent activation of NF-kappaB and ROS formation upon ligand binding. Clin Exp Metastasis 2016;33(6):609–27. [PubMed: 27151304]

Saha A, Lee YC, Zhang Z, Chandra G, Su SB, Mukherjee AB. Lack of an endogenous anti-inflammatory protein in mice enhances colonization of B16F10 melanoma cells in the lungs. J Biol Chem 2010;285(14):10822–31. [PubMed: 20118237]

Sarantou T, Chi DD, Garrison DA, Conrad AJ, Schmid P, Morton DL, et al. Melanoma-associated antigens as messenger RNA detection markers for melanoma. Cancer Res 1997;57(7):1371–6. [PubMed: 9102226]

Shain AH, Bastian BC. The Genetic Evolution of Melanoma. N Engl J Med 2016;374(10):995–6.

Shain AH, Yeh I, Kovalyshyn I, Sriharan A, Talevich E, Gagnon A, et al. The Genetic Evolution of Melanoma from Precursor Lesions. N Engl J Med 2015;373(20):1926–36. [PubMed: 26559571]

Srikrishna G S100A8 and S100A9: new insights into their roles in malignancy. J Innate Immun 2012;4(1):31–40. [PubMed: 21912088]

Surveillance E, and End Results Program. Cancer Stat Facts: Melanoma of the Skin, https://seer.cancer.gov/statfacts/html/melan.html; 2019 [accessed February 24, 2020.2020].

Tekle C, Nygren MK, Chen YW, Dybsjord I, Nesland JM, Maelandsmo GM, et al. B7-H3 contributes to the metastatic capacity of melanoma cells by modulation of known metastasis-associated genes. Int J Cancer 2012;130(10):2282–90. [PubMed: 21671471]

Thrane K, Eriksson H, Maaskola J, Hansson J, Lundeberg J. Spatially Resolved Transcriptomics Enables Dissection of Genetic Heterogeneity in Stage III Cutaneous Malignant Melanoma. Cancer Res 2018;78(20):5970–9. [PubMed: 30154148]

Tirosh I, Izar B, Prakadan SM, Wadsworth MH 2nd, Treacy D, Trombetta JJ, et al. Dissecting the multicellular ecosystem of metastatic melanoma by single-cell RNA-seq. Science 2016;352(6282):189–96. [PubMed: 27124452]

Toki MI, Merritt CR, Wong PF, Smithy JW, Kluger HM, Syrigos KN, et al. High-Plex Predictive Marker Discovery for Melanoma Immunotherapy-Treated Patients Using Digital Spatial Profiling. Clin Cancer Res 2019;25(18):5503–12. [PubMed: 31189645]

Villanueva J, Herlyn M. Melanoma and the tumor microenvironment. Curr Oncol Rep 2008;10(5):439–46. [PubMed: 18706274]

Wagner NB, Weide B, Gries M, Reith M, Tarnanidis K, Schuermans V, et al. Tumor microenvironment-derived S100A8/A9 is a novel prognostic biomarker for advanced melanoma patients and during immunotherapy with anti-PD-1 antibodies. J Immunother Cancer 2019;7(1):343. [PubMed: 31806053]

Wang F, Flanagan J, Su N, Wang LC, Bui S, Nielson A, et al. RNAscope: a novel in situ RNA analysis platform for formalin-fixed, paraffin-embedded tissues. J Mol Diagn 2012;14(1):22–9. [PubMed: 22166544]

Wang Q, Beaumont KA, Otte NJ, Font J, Bailey CG, van Geldermalsen M, et al. Targeting glutamine transport to suppress melanoma cell growth. Int J Cancer 2014;135(5):1060–71. [PubMed: 24531984]

Xiong TF, Pan FQ, Li D. Expression and clinical significance of S100 family genes in patients with melanoma. Melanoma Res 2019;29(1):23–9. [PubMed: 30216200]

Xu S, Yang Z, Zhang J, Jiang Y, Chen Y, Li H, et al. Increased levels of beta-catenin, LEF-1, and HPA-1 correlate with poor prognosis for acral melanoma with negative BRAF and NRAS mutation in BRAF exons 11 and 15 and NRAS exons 1 and 2. DNA Cell Biol 2015;34(1):69–77. [PubMed: 25343173]

Zhang X, Yin M, Zhang LJ. Keratin 6, 16 and 17-Critical Barrier Alarmin Molecules in Skin Wounds and Psoriasis. Cells 2019;8(8).

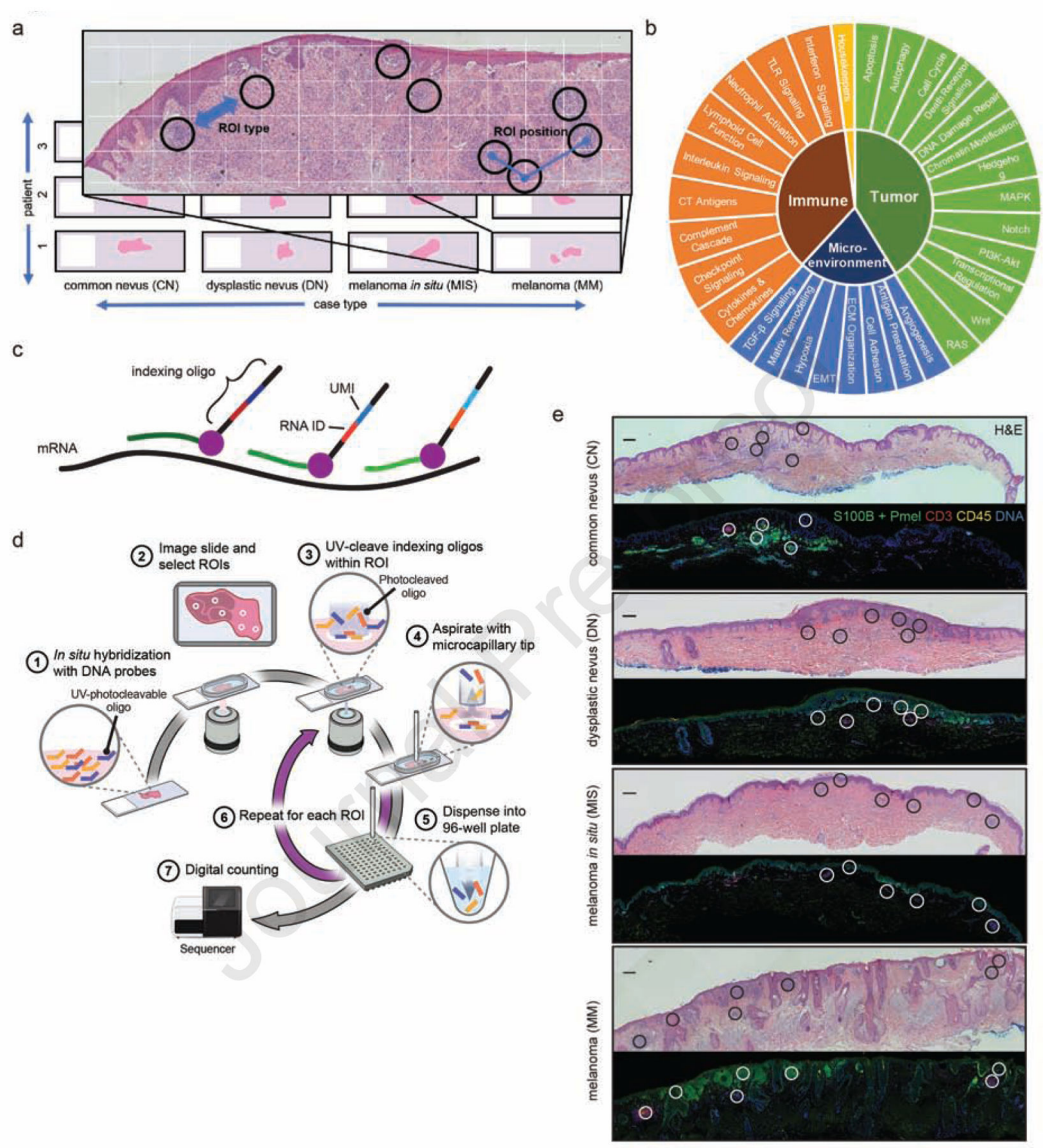

Figure 1. Experimental design for spatially resolving mRNA biomarkers in FFPE samples from four pathologically defined tumor types.

(**a**) Schematic of comparisons enabled by the experimental design (blue arrows). (**b**) Selected pathway content of 1,412-target (4,998-probe) gene panel for DSP with NGS readout. Panel content is approximately 35% immune-related, 40% tumor-related and 20% microenvironment-related, with 1% housekeeping genes and 3% negative probes. (**c**) Schematic of probe design for DSP with NGS readout. Each probe contains an antisense sequence that hybridizes to target mRNA (green), a photocleavable linker (purple), an RNA ID that identifies the mRNA target (red) and a unique molecular identifier (blue) to allow removal of PCR duplicates when converting reads to digital counts. DSP probe pools target each gene with 1–10 probes that hybridize to different sequences along the mRNA transcript and contain >80 negative probes that target scrambled or non-human sequences. (**d**) Workflow for DSP with NGS readout. Collected oligos are PCR-amplified using indexing primers to preserve ROI identity, pooled, purified and sequenced. (**e**) Illustration of

ROI selection process. Top images: ROIs selected by pathologist based on enrichment for melanocytes, keratinocytes or immune cells in H&E section. Bottom images: ROIs collected from a serial section during DSP. Fluorescent antibodies to melanocyte markers S100B and PMEL, T cell marker CD3, lymphocyte marker CD45, and DNA stain SYTO 13 were used as visualization markers during DSP to guide matching of ROIs to the H&E sections. Scale bar = 0.2 mm.

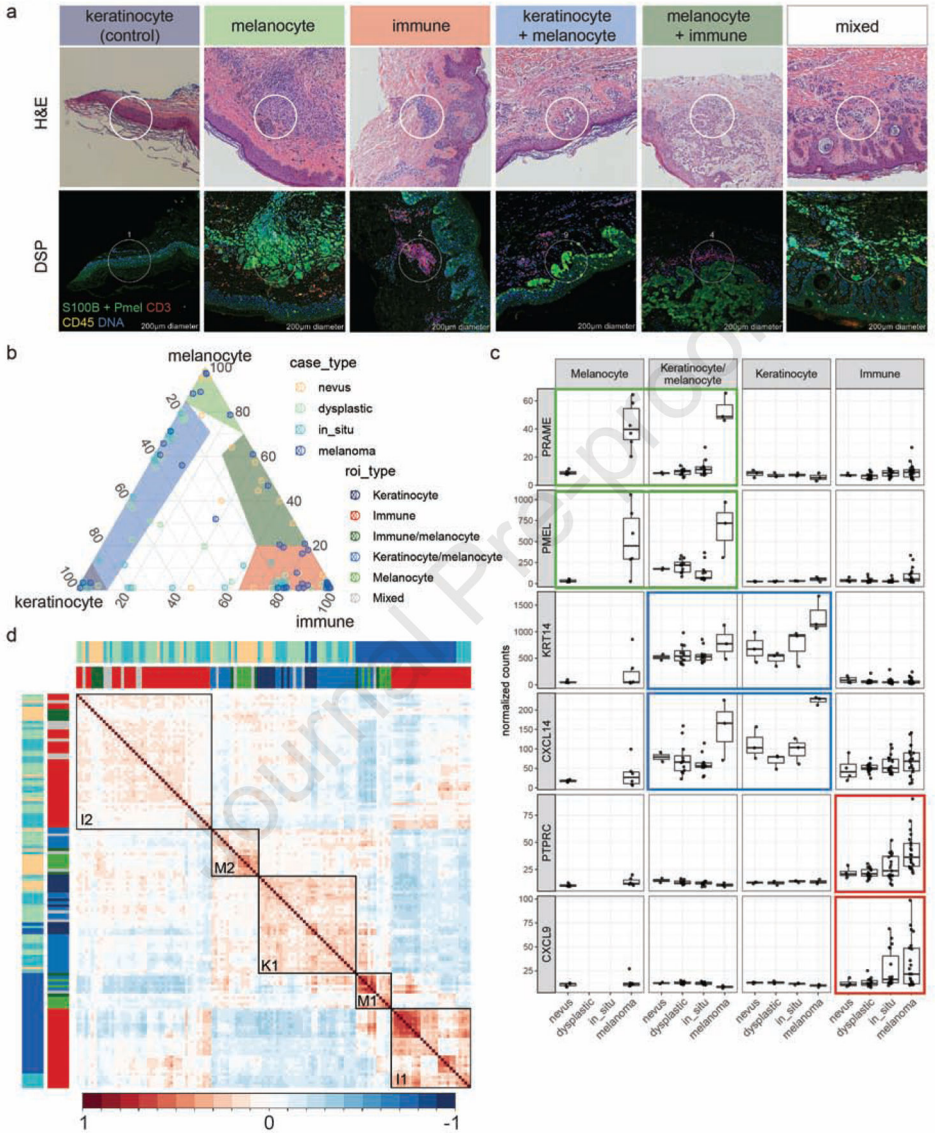

Figure 2. Cell type & tumor type both influence the expression profile of each ROI.

(**a**) Example ROIs for each of the six categories defined in phase II of this study. H&E and matching DSP images are shown. All ROIs selected in this study were 200μm circles. (**a**) Ternary plot displaying cell type composition (% melanocyte, keratinocyte or immune) of each ROI as determined by pathologist evaluation. Shaded regions indicate assignment to the ROI categories shown in (**a**). (**c**) Boxplots of upper quartile-normalized counts by tumor type for selected melanomagenesis-associated genes known to be enriched in melanocytes (green boxes), keratinocytes (blue boxes) or immune infiltrates (red boxes). (**d**) Correlation matrix showing pairwise correlation coefficients (Pearson R) between all ROIs using scaled normalized counts for the 923 genes detected in the experiment (489 genes below the detection threshold in all 134 ROIs were removed prior to clustering). Tumor type and ROI type are indicated by colored bars. The five largest clusters (hclust method) are boxed

and named according to their predominant cell type (M1–2 for melanocyte-rich, I1–2 for immune-rich, K1 for keratinocyte-rich).

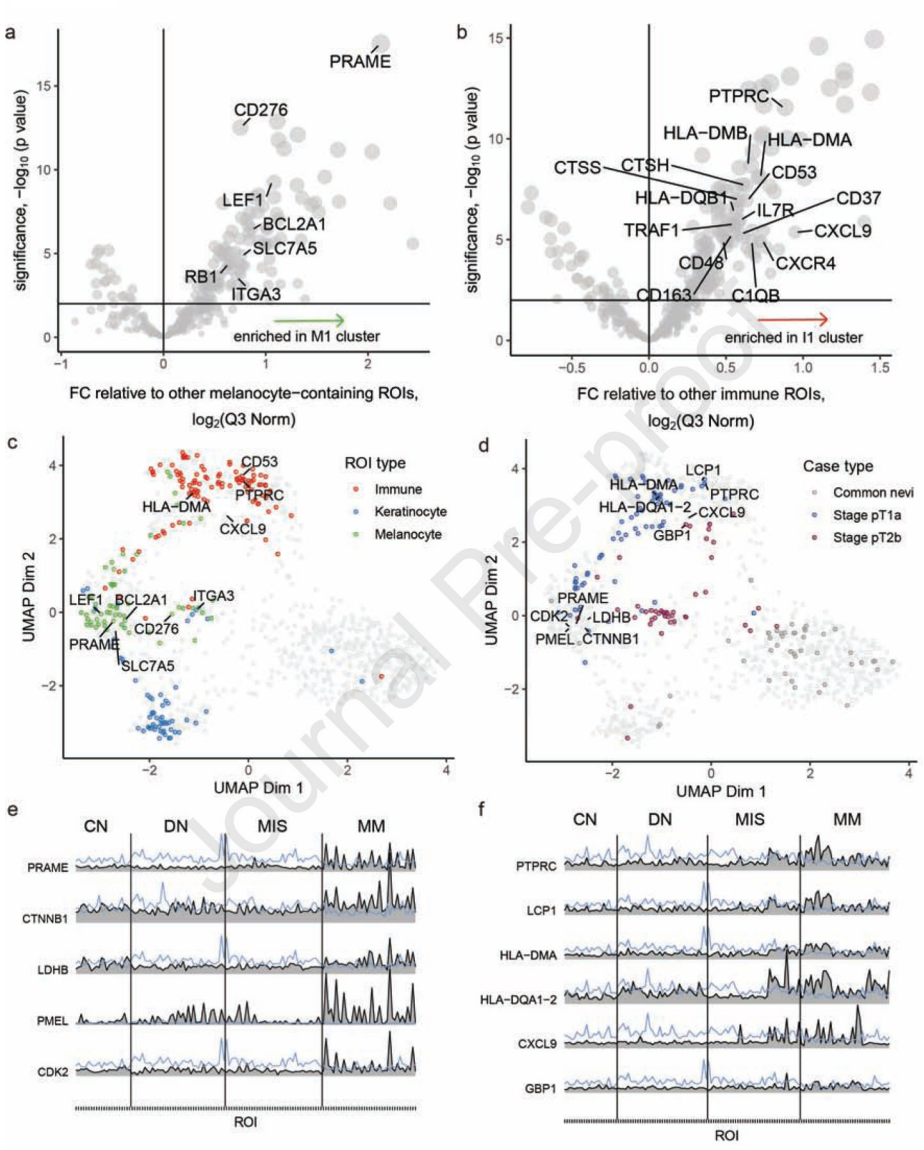

Figure 3. Analysis of M1 and I1 clusters reveals melanoma biomarker candidates.

(**a**) Volcano plot comparing gene expression in M1 ROIs to all other ROIs classified as Keratinocyte-rich, Melanocyte-rich, Keratinocyte/melanocyte or Mixed. Significance (-log10 of p value) was determined by linear regression with a term for random effects from inter-tissue variation. (**b**) Volcano plot comparing gene expression in I1 ROIs to all other ROIs classified as Immune or Immune/melanocyte. Significance (-log10 of p value) was determined by linear regression with a term for random effects from inter-tissue variation. In (**a**) and (**b**), genes were only considered if they were above the detection threshold in at least three ROIs and gene names are only shown if the gene was below the detection threshold in all common nevus ROIs. (**c**-**d**) UMAP analysis comparing the spatial expression profiles of all 923 genes detected in at least one ROI. Colored dots were enriched in the indicated ROI type (**c**) or tumor type (**d**) as determined by linear regression (FDR < 0.01). Top hits from the volcano plots in (**a**-**b**) are indicated in (**c**). Selected genes adjacent to top hits in UMAP

space are indicated in (**d**). (**e-f**) Ridgeline plot of normalized counts for selected genes in all ROIs, organized by tumor type (CN = common nevus, DN = dysplastic nevus, MIS = melanoma in situ, MM = melanoma). Blue line indicates the detection threshold in each ROI.

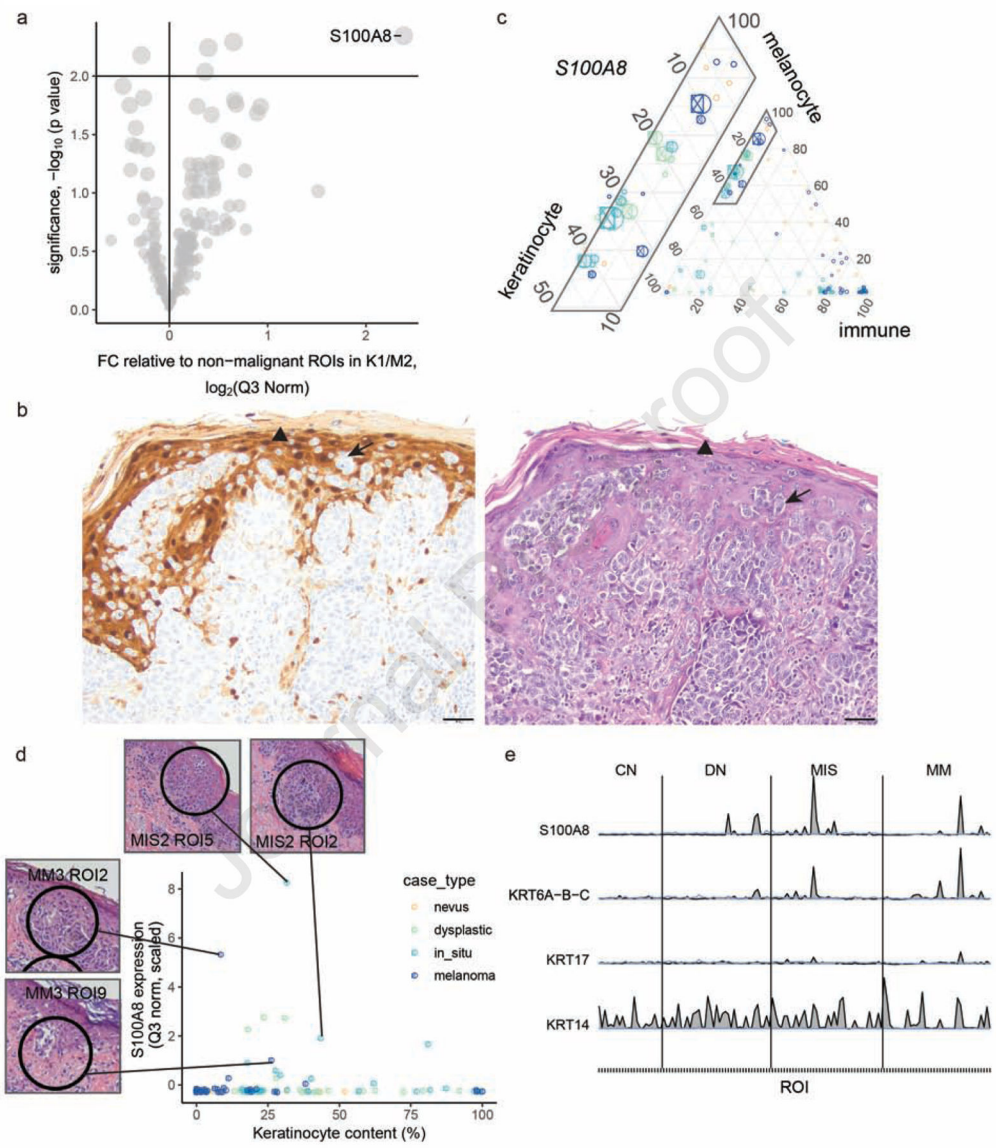

Figure 4. Analysis of K1/M2 clusters reveals enrichment of *S100A8* in keratinocytes during melanomagenesis.

(**a**) Volcano plot comparing gene expression in the subset of ROIs classified as melanoma *in situ* by a pathologist vs. all other ROIs in K1/M2. Significance (-log10 of p value) determined by linear regression with a term for random effects from inter-tissue variation. Genes were only considered if they were above the detection threshold in at least three ROIs, and gene names are only shown if the gene was not detected in any common nevus ROIs. (**b**) Representative IHC image (left panel) and corresponding H&E image (right panel) showing that S100A8 is expressed by keratinocytes (arrowhead) rather than melanocytes (arrow). (**c**) Ternary plot of *S100A8* expression in all ROIs, with a zoomed in view of Keratinocyte/melanocyte ROIs at left. (**d**) H&E images of selected ROIs containing a mixture of keratinocytes and melanocytes. Normalized *S100A8* counts are plotted against keratinocyte score and colored by tumor type. (**e**) Ridgeline plot of normalized counts for

selected genes in all ROIs, organized by tumor type. Blue line indicates LOD in each ROI. Scale bar = 0.05 mm.

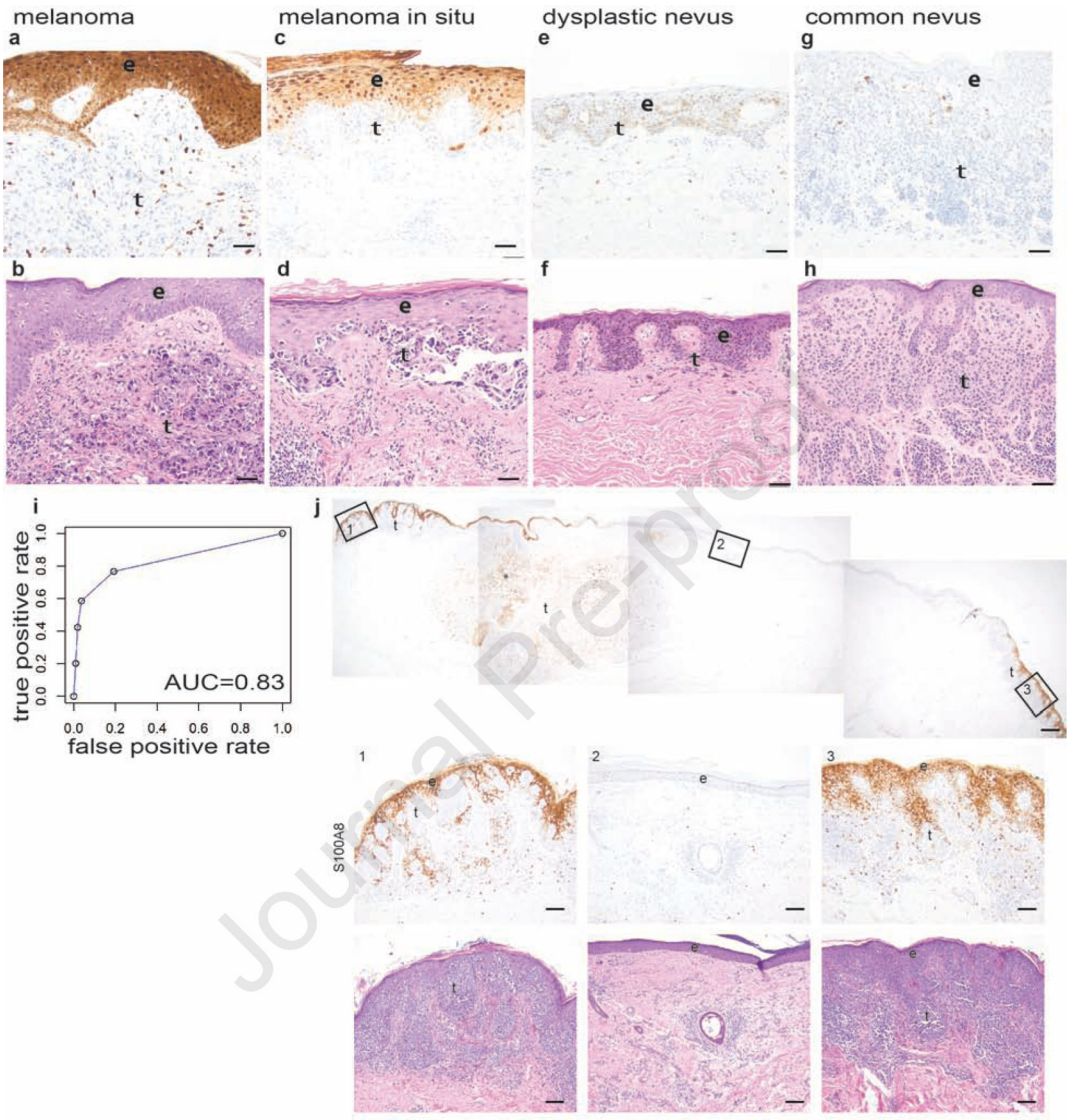

Figure 5. S100A8 is detected in the keratinocyte microenvironment of melanoma

(**a-h**) Representative images of S100A8 IHC (upper panel) and corresponding H&E staining (lower panel) of invasive melanoma in (**a**) and (**b**), melanoma in situ in (**c**) and (**d**), dysplastic nevus in (**e**) and (**f**) and common nevus in (**g**) and (**h**). S100A8 (brown) is expressed by keratinocytes in invasive melanoma in (**a**) and melanoma in situ in (**c**), but not in dysplastic nevus in (**e**) or common nevus in (**g**). (**i**) S100A8 receiver operating characteristic (ROC) curve for in situ or invasive melanoma. AUC, area under the ROC curve. (**j**) Low power image of S100A8 IHC of melanoma with in situ and invasive components and an area of uninvolved skin (upper panel). S100A8 (brown) is expressed by keratinocytes in the epidermis directly associated with melanoma (insets 1 and 3), but not in the uninvolved epidermis (inset 2). Letter “e” indicates epidermal layer containing keratinocytes and letter “t” indicates tumor. Melanin pigment (brown) is present

in dysplastic nevus in (**e**) and in association with invasive melanoma (*) in (**j**). Scale bar = 0.05 mm (**a-h**), scale bar = 0.5 mm (**j**, upper panel), scale bar = 0.1 mm (**j**, insets).

Table 1.

Patient and tumor characteristics of a cohort of 252 tumors stained for S100A8 by immunohistochemistry.

Tumor type	Common nevus N (%)	Dysplastic nevus N (%)	Melanoma in situ N (%)	Invasive melanoma N (%)	Total N (%)
Total	68	66	69	49	252
Sex					
Male	28 (41.2)	35 (53.0)	39 (56.5)	33 (67.3)	135 (53.6)
Female	40 (58.8)	31 (47.0)	30 (43.5)	16 (32.7)	117 (46.4)
Average age (years)	44.1	52.8	62.5	62.2	55.0
Location of tumor					
Face	5 (7.4)	1 (1.5)	10 (14.5)	7 (14.3)	23 (9.1)
Scalp or neck	9 (13.2)	0 (0.0)	5 (7.2)	5 (10.2)	19 (7.5)
Trunk	39 (57.4)	49 (74.2)	22 (31.9)	12 (24.5)	122 (48.4)
Upper extremity	5 (7.4)	11 (16.7)	24 (34.8)	13 (26.5)	53 (21.0)
Lower extremity	10 (14.7)	5 (7.6)	7 (10.1)	12 (24.5)	34 (13.5)
Unknown	0 (0.0)	0 (0.0)	1 (1.4)	0 (0.0)	1 (0.4)
Nevus growth pattern					
Junctional	7 (10.3)	38 (57.6)	n/a	n/a	n/a
Compound	30 (44.1)	28 (42.4)	n/a	n/a	n/a
Intradermal	31 (45.6)	0 (0.0)	n/a	n/a	n/a
Invasive melanoma average tumor thickness (mm)	n/a	n/a	n/a	2.33	n/a
Invasive melanoma ulceration present	n/a	n/a	n/a	5 (10.2)	n/a
Primary tumor stage					
Tis	n/a	n/a	69	n/a	n/a
T1a	n/a	n/a	n/a	29 (59.2)	n/a
T1b	n/a	n/a	n/a	5 (10.2)	n/a
T2a	n/a	n/a	n/a	2 (4.1)	n/a
T2b	n/a	n/a	n/a	2 (4.1)	n/a
T3a	n/a	n/a	n/a	5 (10.2)	n/a
T3b	n/a	n/a	n/a	1 (2.0)	n/a
T4a	n/a	n/a	n/a	3 (3.1)	n/a
T4b	n/a	n/a	n/a	2 (4.1)	n/a

Table 2.

S100A8 expression in a cohort of 252 tumors.

Tumor type	Common nevus N (%)	Dysplastic nevus N (%)	Melanoma in situ N (%)	Invasive melanoma N (%)	Total N (%)	P-value*
Total	68	66	69	49	252	
S100A8 IHC score						.001
Score 1 (0–4%)	51 (75.0)	48 (72.7)	21 (30.4)	3 (6.1)	123 (48.8)	
Score 2 (5–25%)	15 (22.1)	13 (19.7)	13 (18.8)	7 (14.3)	48 (19.0)	
Score 3 (26–50%)	1 (1.5)	2 (3.0)	8 (11.6)	10 (20.4)	21 (8.3)	
Score 4 (51–75%)	0 (0.0)	2 (3.0)	19 (27.5)	12 (24.5)	33 (13.1)	
Score 5 (> 75%)	1 (1.5)	1 (1.5)	8 (11.6)	17 (34.7)	27 (10.7)	

*Pearson Chi-Square

**% of epidermis associated with tumor stained: 1= 0–5%; 2= 6% to 25%; 3= 26% to 50%; 4= 51% to 75%; 5= >75%